CONDENSED MATTER PHYSICS

A simple electron counting model for half-Heusler surfaces

Jason K. Kawasaki,[1,2]* Abhishek Sharan,[3] Linda I. M. Johansson,[2,4] Martin Hjort,[5] Rainer Timm,[5] Balasubramanian Thiagarajan,[6] Brian D. Schultz,[7] Anders Mikkelsen,[5] Anderson Janotti,[3,8] Chris J. Palmstrøm[2,7]*

Heusler compounds are a ripe platform for discovery and manipulation of emergent properties in topological and magnetic heterostructures. In these applications, the surfaces and interfaces are critical to performance; however, little is known about the atomic-scale structure of Heusler surfaces and interfaces or why they reconstruct. Using a combination of molecular beam epitaxy, core-level and angle-resolved photoemission, scanning tunneling microscopy, and density functional theory, we map the phase diagram and determine the atomic and electronic structures for several surface reconstructions of CoTiSb (001), a prototypical semiconducting half-Heusler. At low Sb coverage, the surface is characterized by Sb-Sb dimers and Ti vacancies, while, at high Sb coverage, an adlayer of Sb forms. The driving forces for reconstruction are charge neutrality and minimizing the number of Sb dangling bonds, which form metallic surface states within the bulk bandgap. We develop a simple electron counting model that explains the atomic and electronic structure, as benchmarked against experiments and first-principles calculations. We then apply the model to explain previous experimental observations at other half-Heusler surfaces, including the topological semimetal PtLuSb and the half-metallic ferromagnet NiMnSb. The model provides a simple framework for understanding and predicting the surface structure and properties of these novel quantum materials.

INTRODUCTION

The properties at surfaces and at the interfaces between two different materials are often inherently different from that of their bulk constituents. This idea lies at the heart of quantum material heterostructures, whereby new phenomena emerge at the interface between two materials with different functionality (*1*) or at the interface between a material and the vacuum [that is, a surface (*2*, *3*)]. Among these quantum materials, the family of so-called full- and half-Heusler intermetallic compounds (stoichiometry X_2YZ or XYZ, respectively) is a particularly promising platform. These materials exhibit a diverse range of tunable properties including topological states (*2*–*4*), half-metallic ferromagnetism (*5*), superelasticity (*6*), shape memory effect (*7*), novel superconductivity (*8*), and Weyl fermions (*9*); and they are well lattice- and symmetry-matched to technologically important compound semiconductor substrates (*10*). The properties at these surfaces and interfaces are inherently tied to their atomic structures, making knowledge and control of surface/interface structure a necessary prerequisite to determining real properties. However, despite the growing body of experimental evidence that Heusler surfaces and interfaces reconstruct (*11*–*15*), their origins, atomic structures, and direct effects on properties are not understood.

The challenges are twofold. First, measuring the surface/interface structure requires the ability to reproducibly fabricate and control a particular structure and to couple the sample fabrication with surface-sensitive probes. Second, from a theoretical viewpoint, the low-energy structure is often too difficult to determine from first principles alone: At surfaces/interfaces, the symmetry is reduced, atoms have increased degrees of freedom, and unit cells can be many times larger than that of the bulk. For these reasons, most theoretical treatments of Heusler heterostructures rely on idealized slabs with (1 × 1) periodicity (*16*, *17*). Direct measurements of atomic structure, as well as simple models to explain their behavior, are needed to guide among all possible atomic configurations.

One powerful framework for understanding surface reconstructions is electron counting, which successfully predicts the stable atomic structures of many group III-V and II-VI compound semiconductor surfaces (*18*). These surfaces tend to reconstruct such that the number of energetically unfavorable dangling bonds is minimized. The remaining dangling bonds on the more electronegative species (V or VI) are expected to be doubly occupied, while dangling bonds on the electropositive species (III or II) are expected to be empty (*18*). These simple arguments provide a powerful means to quickly and efficiently screen among possible structures. Select candidates can then be analyzed more in depth by perturbative density functional theory (DFT)–based methods (*19*). However, it is not clear whether a similarly simple framework could apply for Heuslers. Heuslers are ternary compounds with even more configurational degrees of freedom than binary semiconductors, their crystal structures are more complex, and their bonding interactions are p-d as opposed to simple s-p. But it is precisely this configurational complexity that would make a simple and intuitive model even more valuable for Heuslers than it has been for compound semiconductors, as a method to screen over an even greater landscape of potential structures.

Here, we present a combined experimental and theoretical study of the half-Heusler CoTiSb (001) surface. CoTiSb is a semiconducting, high figure-of-merit thermoelectric material and building block for all-Heusler–based spintronic and topological heterostructures. We experimentally map the surface phase diagram and determine the atomic and electronic structures for the $c(2 \times 4)$, (2×1), and (1×4) reconstructions of our molecular beam epitaxy (MBE)–grown films. These surfaces are

[1]Department of Materials Science and Engineering, University of Wisconsin–Madison, Madison WI 53706, USA. [2]Materials Department, University of California, Santa Barbara, Santa Barbara, CA 93106, USA. [3]Department of Physics and Astronomy, University of Delaware, Newark, DE 19716, USA. [4]Nanometer Structure Consortium, Lund University, Lund, Sweden. [5]Division of Synchrotron Radiation Research and Nanometer Structure Consortium, Lund University, Lund, Sweden. [6]MAX IV Laboratory, Lund University, Lund, Sweden. [7]Department of Electrical and Computer Engineering, University of California, Santa Barbara, Santa Barbara, CA 93106, USA. [8]Department of Materials Science and Engineering, University of Delaware, Newark, DE 19716, USA.
*Corresponding author. Email: jkawasaki@wisc.edu (J.K.K.); cpalmstrom@ece.ucsb.edu (C.J.P.)

characterized by Sb-Sb dimers and Ti vacancies at low Sb coverage and an adlayer of Sb at high Sb coverage, as revealed by in situ x-ray photoemission spectrsoscopy (XPS) and scanning tunneling microscopy (STM) and synchrotron-based core and angle-resolved photoemission spectroscopy (ARPES). We develop a simple electron counting model that captures the atomic and electronic structure of CoTiSb (001), as benchmarked against experiments and first-principles DFT calculations. The accuracy of the model is quite remarkable, given the more complicated stoichiometry, bonding, valence structure, and crystal structure of Heuslers as compared with group III-V semiconductors. Finally, we apply the model to explain previously observed changes in stoichiometry, spin polarization, and electronic states at other half-Heusler surfaces, including the half-metallic NiMnSb and the topological semimetal PtLuSb. Our model provides a simple framework to understand and predict surface structure and properties in these novel quantum materials.

The bulk MgAgAs-type (half-Heusler) crystal structure consists of three interpenetrating face-centered cubic (fcc) sublattices with elements *X* (Co), *Y* (Ti), and *Z* (Sb) at $(\frac{1}{4},\frac{1}{4},\frac{1}{4})$, $(\frac{1}{2},0,0)$, and (0, 0, 0), respectively, where *Z* is typically the most electronegative species, and *Y* is the most electropositive species (Fig. 1). This structure can be viewed as a zincblende *XZ* (CoSb) sublattice that is "stuffed" with *Y* (Ti) at the octahedral sites (*20*, *21*) or as a rocksalt *YZ* (TiSb) sublattice stuffed with *X* (Co) at the tetrahedral sites (*22*).

Real-space electronic structure calculations suggest that bonding interactions within the zincblende sublattice are covalent (*20*), while interactions within the rocksalt sublattice are ionic (*22*). By contrast, many of the closely related full-Heuslers (related by addition of a fourth fcc sublattice *X′*) are well described by a metallic bonding picture (*23*). For half-Heuslers, the valence electron count is important: While these compounds exist over a range of electron counts, those with 18 valence electrons per formula unit ($s^2 + p^6 + d^{10}$, ; that is, filled orbitals) are in greatest abundance and tend to have a semiconducting bandgap. Those with greater or fewer valence electrons tend to be metallic and magnetic (*20*). In (001) orientation, the structure consists of alternating atomic planes of *X* (Co) and *YZ* (TiSb). Hence, an unreconstructed CoTiSb surface is expected to be either Co- or TiSb-terminated.

RESULTS

Reconstruction phase diagram

Experimentally, we observe a number of reconstructions that deviate from the simple bulk-like termination. Figure 2 presents an experimental phase diagram and low-energy electron diffraction (LEED) patterns for our MBE-grown CoTiSb (001) films as a function of postgrowth anneal temperature and Sb flux (see Materials and Methods and fig. S1). Starting from the (2 × 1), which is the reconstruction observed during growth, a $c(2 \times 4)$ appears for high-temperature/low–Sb-flux conditions and a progression to a (1 × 4), and then, an Sb-capping regime appears at lower temperature/higher Sb flux. The (2 × 1) → $c(2 \times 4)$ phase transition occurs only in one direction upon heating, suggesting that in some regions of the apparent experimental phase diagram, the (2 × 1) may be metastable, with the $c(2 \times 4)$ being the true minimum.

This strong dependence of CoTiSb (001) surface reconstruction on Sb flux and anneal temperature is surprisingly similar to the behavior of zincblende III-V semiconductors, for example, GaAs and GaSb (001), for which the temperature and group V flux determine the relative rates of group V adsorption or desorption. For GaAs and GaSb, the 2 × periodicity at low group V flux results from Sb-Sb or As-As dimerization (*18*), and a similar Sb-Sb dimerization may be responsible for the $c(2 \times 4)$ and (2 × 1) reconstructions of CoTiSb. At higher group V flux and lower temperature, GaAs and GaSb surfaces are characterized by an adlayer of As or Sb on the surface (*24*), and similar behavior may occur for the CoTiSb (1 × 4).

Here, we will show that the mechanisms for reconstructions are indeed similar. Despite the more complicated stoichiometry, bonding, and crystal structure for half-Heuslers, the reconstructions can be described in similar terms of electron counting in a "stuffed zincblende" lattice. This treatment yields new conditions for the surface stoichiometry at the "stuffing" Y (Ti) site and for the filling of Z (Sb) site dangling bonds.

Stoichiometry and bonding

Photoemission spectroscopy measurements support the picture of Sb-Sb dimerization for the $c(2 \times 4)$ and (2 × 1) and an Sb adlayer for the (1 × 4). Figure 2C shows the integrated intensity ratios $(I_x/I_{Co2p})_{(n \times m)}/(I_x/I_{Co2p})_{(2 \times 1)}$,

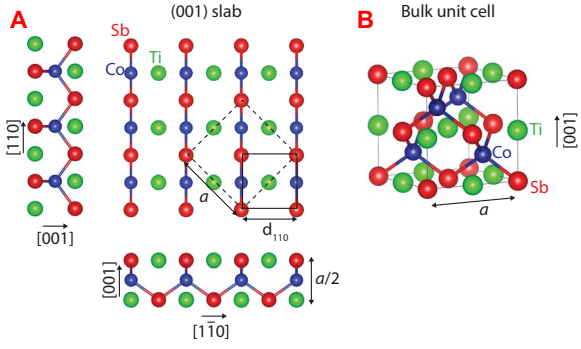

Fig. 1. Crystal structure of CoTiSb. (**A**) Unrelaxed (001) slab of CoTiSb with TiSb termination. The conventional bulk unit cell is marked by dashed lines (edge length *a*), and the (1 × 1) surface unit cell is marked by a solid line. (**B**) Conventional cubic unit cell consisting of a CoSb zincblende sublattice that is stuffed with Ti.

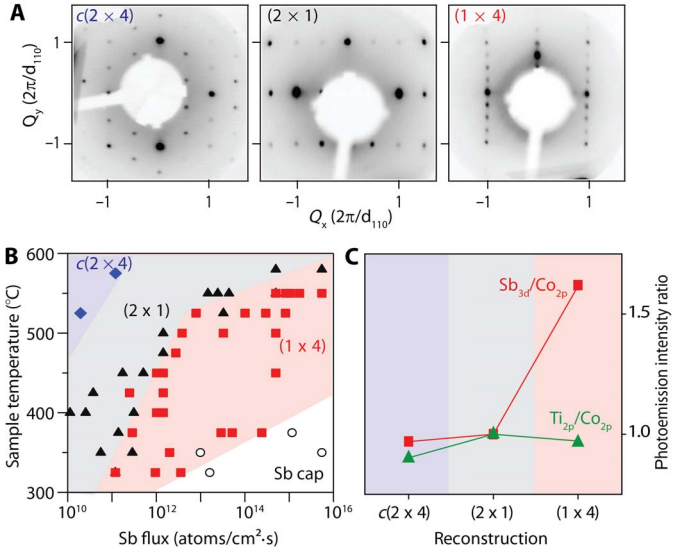

Fig. 2. Surface reconstructions of CoTiSb (001). (**A**) LEED patterns for the $c(2 \times 4)$, (2 × 1), and (1 × 4) reconstructions ($Q_x||[1\bar{1}0]$, $Q_y||[110]$). (**B**) Experimental phase diagram as a function of sample anneal temperature and Sb flux. (**C**) Photoemission intensity ratios Sb_{3d}/Co_{2p} and Ti_{2p}/Co_{2p}, normalized to the ratio for the (2 × 1).

as extracted from in situ photoemission measurements (where x = Sb 3d or Ti 2p; raw data in fig. S1). We use a ratio of ratios to cancel out the photoemission cross section and instrument-dependent factors (see Materials and Methods). Hence, this ratio of ratios describes a relative change in Sb or Ti stoichiometry from the as-grown (2 × 1) surface. Fitting the relative changes to a layer attenuation model (see Materials and Methods), we find that the (1 × 4) is characterized by an excess ≈ 1.5 monolayer (ML) of Sb on the surface, as compared to the nominally TiSb-terminated (2 × 1). The $c(2 \times 4)$ has a similar Sb stoichiometry as the (2 × 1) but has ≈ 0.3 MLs less Ti at the surface (that is, more Ti vacancies).

For a clearer understanding of the surface bonding, we perform higher-resolution synchrotron photoemission measurements at beamline I311 of MAX-LAB, using an Sb-capping scheme to protect the sample surfaces during transfer (see Materials and Methods). Figure 3A presents measurements of the Sb 4d core level for a $c(2 \times 4)$ sample. At $h\nu$ = 950 eV, we observe the two spin-orbit split Sb $4d_{5/2}$ and $4d_{3/2}$ core levels at 31.9 and 33.2 eV, respectively. As the incident photon energy is decreased and the measurement becomes more surface-sensitive, we observe a screened secondary component at lower binding energy. We attribute this secondary component to surface Sb-Sb dimerization, consistent with the binding energy shift observed for the Sb-Sb (As-As)–dimerized surfaces of GaSb (GaAs) (*24*).

To further assess the bonding and formal charges on each species, we perform an angle-integrated photoemission measurement of the valence bands (Fig. 3B, black dots). The energy positions are in good agreement with the DFT-projected densities of states (DOSs) for bulk CoTiSb (shaded) using the generalized gradient approximation (GGA) (see Materials and Methods). The low-lying states from 6 to 3 eV have primarily Sb 5p character, the states in the upper valence band from 2.5 to 0.6 eV have primarily Co 3d character, and the unoccupied conduction bands have primarily Ti 3d character. From the orbital projected DFT band dispersions (fig. S2), we find strong hybridization of Sb-Co p-d and Co-Ti d-d. Together, our calculations and measurements support a nominal picture of the Co and Sb states being fully occupied (Sb s^2p^6, and Co d^{10}) and Ti unoccupied (d^0), leading to a bulk bandgap at the Fermi level and formal charges of Sb^{3-}, Co^{1-}, and Ti^{4+}. These formal charges support the picture of a zincblende $CoSb^{4-}$ sublattice that is isostructural and isoelectronic with zincblende GaSb and stuffed with Ti^{4+}, consistent with previous theoretical studies (*20*). Here, CoTiSb may be viewed as a ternary cousin to groups III-V such as GaSb but where the gap is across d states rather than s-p states (further discussion in note S1 and fig. S2).

In addition to these bulk features, we also observe finite spectral weight at the Fermi level (0 eV) within the bulk bandgap. We attribute these features to metallic surface states, as our measurement at $h\nu$ = 70 eV is extremely surface-sensitive ($\lambda_{IMFP} \approx 5$ Å), and ARPES measurements reveal that they have two-dimensional dispersion.

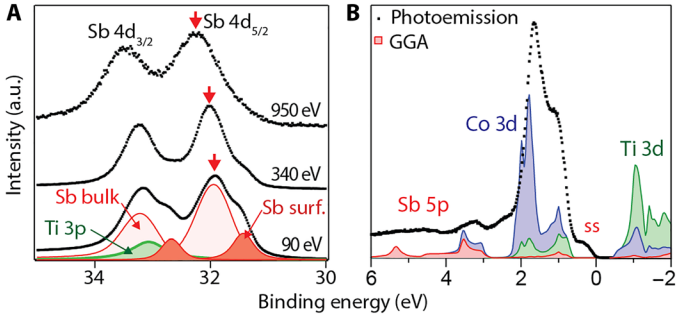

Fig. 3. Bonding and electronic structure of the $c(2 \times 4)$ as revealed by higher-resolution synchrotron photoemission. (**A**) Sb 4d core level as a function of decreasing incident photon energy from $h\nu$ = 950 eV [inelastic mean free path $\lambda_{IMFP} \approx 20$ Å] to $h\nu$ = 90 eV ($\lambda_{IMFP} \approx 5$ Å). a.u., arbitrary units. (**B**) Surface-sensitive measurement of the valence band ($h\nu$ = 70 eV; black dots) showing good agreement with the DFT-projected DOS (shaded). We observe finite spectral weight at the Fermi level (0 eV) within the bulk gap, which we attribute to surface states (ss).

Atomic structure and comparison with theory

We verify the structure of proposed Sb-Sb dimer and adlayer reconstructions using a combination of real-space imaging and first-principles calculations. Figure 4 (A and B) shows in situ filled-state STM images of (i) a sample with (2 × 1) and $c(2 \times 4)$ termination and (ii) a sample with (1 × 4) termination. The real-space topography of the (2 × 1)/$c(2 \times 4)$ surface is consistent with Sb-Sb dimerization. Here, the surface is characterized by clusters that are 8.2 Å in width along $[1\bar{1}0]$, the same direction and 2 × spacing expected for Sb-Sb dimers. The (2 × 1) regions are characterized by [110]-oriented rows of this structure, while the $c(2 \times 4)$ regions are a checkerboard pattern of this structure.

The (1 × 4) surface (Fig. 4B), which is produced under Sb-rich conditions, is characterized by rows of three atoms, followed by a trench, suggesting an Sb adlayer coverage of 0.75 ML. The measured step height of this adlayer is also consistent with 0.75 ML Sb coverage: At some step edges, the sample contains small regions of (2 × 1) termination. The measured step heights across (1 × 4) and (2 × 1) phase boundaries are 1.5 Å (≈ a/4), the same height expected for single-layer Sb/TiSb steps (fig. S4).

To investigate the stability of the proposed Sb dimer and adlayer reconstructions, we perform DFT calculations using 4 × 4 slab supercells with a thickness of 13 atomic layers, separated by 12 Å of vacuum (see Materials and Methods). We perform relaxation of four layers near the surface, allowing the Sb atoms on the surface to dimerize and look for changes in the reconstruction and dimer formation by varying the Ti content in the top-most TiSb layer, with Ti coverage varying from zero (n_{Ti} = 0) to full occupancy (n_{Ti} = 1), in steps of Δn_{Ti} = 1/16. For each value of n_{Ti}, we sample all symmetry-unique Ti vacancy configurations available in the 4 × 4 supercell. We also consider an Sb adlayer for varying Sb adlayer coverage and varying n_{Ti}.

The calculated phase diagram is shown in Fig. 4E, along with several corresponding structural models and simulated filled-state STM images (Fig. 4, D and C). Models for the remaining (not experimentally observed) reconstructions are shown in fig. S5. For high Ti chemical potential, we find a fully stoichiometric TiSb-terminated surface, the β − (1 × 1), in which there are no in-plane displacements and only minor (< 20 pm) out-of-plane bucklings. The α − (1 × 1) has two missing Ti per 4 × 4 cell, with slight (< 20 pm) in-plane displacements of Sb nearest neighbors to the vacant site. Decreasing μ_{Ti} even further, Sb-Sb dimerization becomes energetically favorable, as exhibited by the (2 × 1) and $c(2 \times 4)$ reconstructions. Finally, at a very high Sb chemical potential, a 0.75 Sb adlayer (1 × 4) is stable.

In the naming of these calculated reconstructions, particularly, the (2 × 1), we ignore the apparent ordering of Ti vacant sites for two reasons. First, our calculations reveal that ordered rows of Sb-Sb dimers are stable over a range of Ti compositions. Second, for a given value of n_{Ti}, the differences in formation energy between different Ti vacancy configurations are quite small, suggesting that the real structures have disordered arrangements of Ti vacancies. For example, the two lowest-energy configurations for n_{Ti} = 3/8 differ by only 4 meV per surface Sb

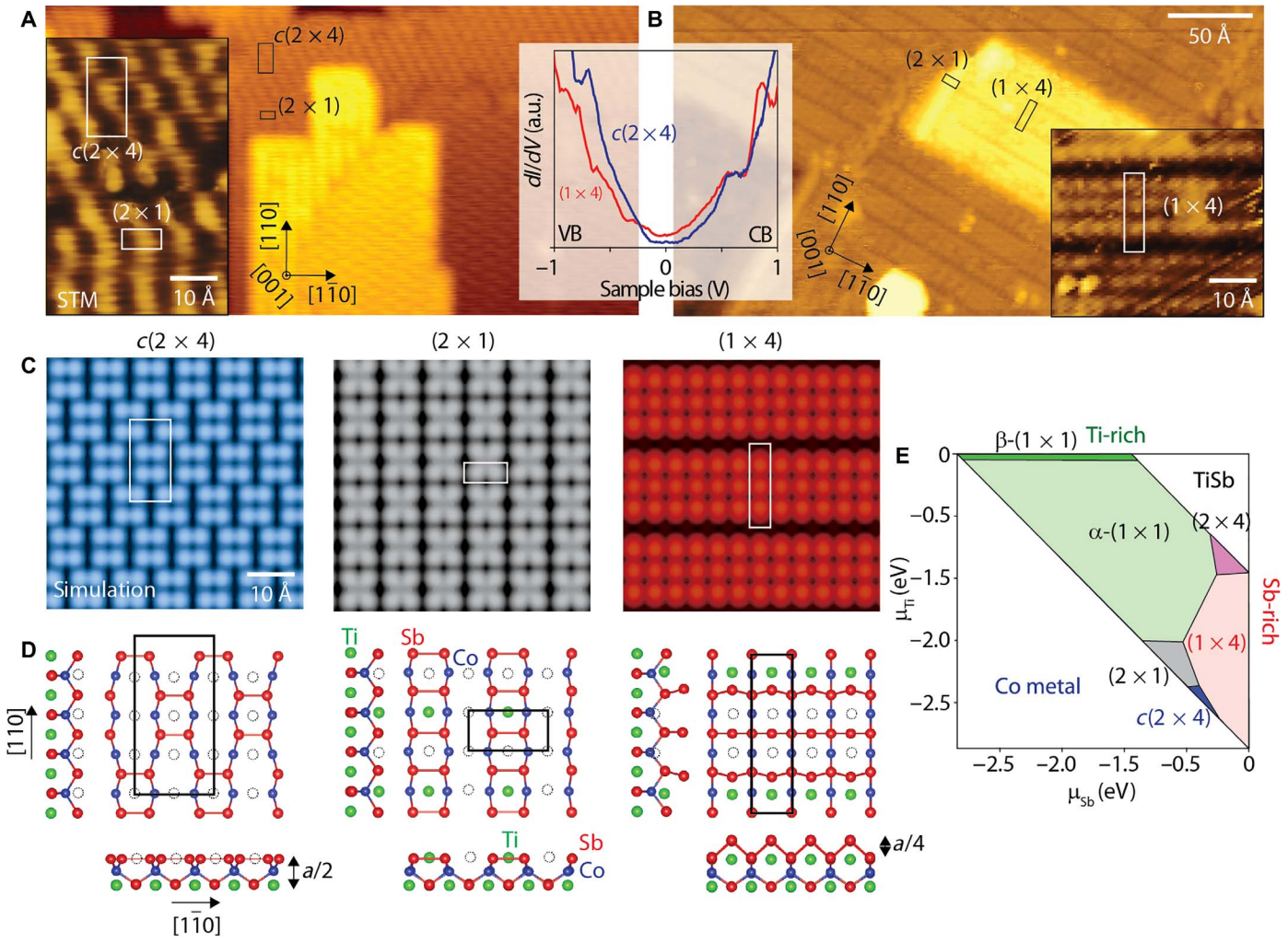

Fig. 4. Real-space imaging of the CoTiSb (001) surface. (**A** and **B**) Filled-state STM images of the reconstructions (−1.5-V sample bias, 300-pA tunnel current, 350 × 184 Å^2). The (2 × 1)/*c*(2 × 4) sample was grown using an ErAs diffusion barrier; hence, there are 90° rotational domains. The (1 × 4) sample was grown directly on InAlAs, and hence, there are no rotational domains. The middle inset shows differential conductance spectra for (1 × 4) and *c*(2 × 4) regions, with both spectra showing a finite minimum of metallic surface states at the Fermi level (0 V). VB denotes valence band, CB denotes conduction band. (**C** and **D**) Simulated STM images (C) and the corresponding relaxed atomic models (D) as calculated by DFT. Open circles denote Ti vacancies. For the purposes of comparison to experiment, in our naming of the reconstructions, we do not consider superstructure ordering on the Ti vacancy sites. (**E**) Surface reconstruction phase diagram calculated by DFT as a function of Ti and Sb chemical potential.

atom, much smaller than the thermal energy $k_BT \approx 25$ meV at room temperature. Therefore, we expect most real structures at finite temperature to have a disordered arrangement of Ti vacancies, and the apparent order in slab calculations results only from the use of a finite supercell with periodic boundary conditions.

The calculated reconstructions are in agreement with all experimental data, both in terms of their structure and their relative positions in the phase diagram. The (1 × 4), which is experimentally observed for Sb-rich annealing conditions, appears in the calculated phase diagram at high μ_{Sb}. The 0.75 ML adlayer of Sb in the DFT calculations is consistent with the 0.75 ML estimate from STM and the 1.5-ML estimate from photoemission. We attribute the overestimate from photoemission to spatial inhomogeneities in the sample, for example, regions of excess Sb capping on an otherwise nominally (1 × 4) reconstructed surface.

Meanwhile, the (2 × 1) and *c*(2 × 4), which appear experimentally during growth or during annealing at high temperature/low Sb flux, appear at lower μ_{Sb} in the calculated phase diagram. The stable structures in DFT are characterized by Sb-Sb dimers, consistent with the Sb 4d core-level shift in photoemission (Fig. 3) and clustering in STM. The difference between these two dimer reconstructions is the long-range ordering: rows of dimers for the (2 × 1) and a checkerboard for the *c*(2 × 4). For CoTiSb, the *c*(2 × 4) is energetically favored for 0 Ti coverage in the top layer (Fig. 4D), while a (2 × 1) exists over a range of Ti compositions. This is consistent with photoemission measurements suggesting that, while the Sb composition of the two reconstructions is comparable, the *c*(2 × 4) is more Ti-deficient (Fig. 2). More detailed comparisons between the measured STM line profiles and the proposed models are shown in fig. S4, which also show excellent agreement.

A minor discrepancy is that DFT predicts the *c*(2 × 4) will form in more Sb-rich conditions than the (2 × 1) (Fig. 4E), while the opposite apparent trend was observed experimentally (Fig. 2). We attribute this discrepancy to a combination of kinetics, disorder, and finite temperature

effects that are not accounted for in a DFT-based equilibrium phase diagram. Our calculations reveal that, within the nominal $c(2 \times 4)$ stability region, the $c(2 \times 4)$ is lower than the (2×1) by only 8 meV per surface functional unit (fig. S5B). This small energy may explain two sets of experimental observations. First, the real system annealed at finite temperature is often a mix of (2×1) and $c(2 \times 4)$ regions, as observed in our STM measurements (Fig. 4 and fig. S4). Second, our annealing experiments revealed that a (2×1) to $c(2 \times 4)$ phase transition is observed only in one direction upon heating, and the reverse is not observed upon cooling. The very small calculated energy difference between the two reconstructions across a range of chemical potentials suggests that in some regions, the (2×1) may actually be metastable, requiring additional energy to overcome kinetic barriers and fall into the lowest-energy $c(2 \times 4)$ structure. Therefore, the experimentally constructed phase diagram likely overestimates the true size of the (2×1) region and underestimates the size of the $c(2 \times 4)$ region. These kinetic factors likely explain the apparent reordering of the $c(2 \times 4)$ and (2×1) in the experiment, in which the $c(2 \times 4)$ is better viewed as a high-temperature reconstruction, rather than as an Sb-rich reconstruction.

Surprisingly, our DFT calculations suggest that Sb-Sb dimers are only stable for surfaces with a significant fraction of missing Ti in the top layer and are unstable for full Ti coverage. This indicates that there must be a strong driving force both for Sb dimerization and for decreasing the surface Ti composition.

Electron counting model

We argue that the driving forces for these reconstructions are (i) minimizing the number of energetically unfavorable dangling bonds and (ii) maintaining charge neutrality at the surface. We explain these trends using a simple electron counting model. In the bulk, we treat each species as having formal charges Co^{1-} (d^{10}), Sb^{3-} (s^2p^6), and Ti^{4+} (d^0), consistent with our valence band photoemission measurement and DFT-projected DOS (Fig. 3B and fig. S2). This is also consistent with the familiar 18 valence electron condition commonly applied to bulk half-Heuslers (*20*). Now focusing on the surface, stability and charge neutrality dictate that the number of electrons at the surface required by the structure (bonding) equals the number of electrons available from the stoichiometry.

We first apply the count to an unrelaxed, stoichiometric TiSb-terminated surface to show that this surface is unstable; that is, it does not satisfy the electron count. In (001) orientation, CoTiSb consists of alternating atomic layers of TiSb and Co (Fig. 1), with formal charges 1+ and 1−, respectively. Here, the TiSb layers formally donate half an electron each to the Co layers above and below. This results in an excess of half an electron per formula unit at a TiSb-terminated surface, which is energetically unfavorable. In a bonding picture, there are two dangling bonds per Sb atom at the surface (Fig. 5B), which is also energetically unfavorable.

The surface can lower its energy by hybridizing half of the dangling bonds into Sb-Sb dimers. Charge neutrality can be satisfied by decreasing the surface Ti coverage, since Ti^{4+} is a donor to the zincblende $CoSb^{4-}$ sublattice. Consider a dimerized surface (Fig. 5A) in which we allow for a fractional coverage of Ti (n_{Ti}) in the top-most TiSb layer. We now apply the count to the smallest surface unit cell that can support a dimer, a (2×1). Note that the same count applies to $c(2 \times 4)$ cell since the two reconstructions are staggered variants of one another. The (2×1) cell contains one Sb-Sb dimer bond, two Sb dangling bonds, and four Co-Sb back bonds. This tetrahedral bonding picture for the p-d hybridized $CoSb^{4-}$ sublattice is consistent with real-space electronic structure calculations (*20*). Filling up these bonds requires a total of 2 (Sb dimer) + 8 (CoSb back) + 4 (Sb dangling) + 10 (Co d^{10}) = 24 electrons per (2×1) cell, assuming that each Sb dangling bond is fully occupied (2 electrons) since Sb is the most electronegative species. This condition is analogous to the well-studied III-V semiconductor surfaces such as the GaAs (001) – (2×4) (*18*) and results in a formally charge neutral surface that is expected to be semiconducting. Alternatively, allowing for Jahn-Teller–like distortions that would split the degeneracy of Sb dangling bond states on either side of the dimer (for example, by dimer buckling), this would require half-filling of the Sb dangling bonds, for a total of 22 electrons required per cell. This is analogous to the out-of-plane dimer buckling observed in the Si (001)–(2×1) (*25*). The bond filling can also be visualized in our schematic surface DOS (Fig. 5E), in which filled bands (bonds) are below the Fermi level.

Now, consider the number of electrons available: 2×5 from Sb at the top layer, $2 \times 4 \times n_{Ti}$ from Ti at the top layer (n_{Ti} is the fractional occupancy of Ti at the surface), and $2 \times \frac{9}{2}$ from Co at the second layer, where we have divided by two to avoid double counting the Co, which formally contributes half of its electrons each to the layer above and the layer below. This results in a total of $19 + 8n_{Ti}$ electrons available. Equating the numbers of electrons required and available, we find that the count is satisfied and that dimerized surfaces should be stable for a Ti coverage of $n_{Ti} = 3/8$ for half-filling of the Sb dangling bonds and $n_{Ti} = 5/8$ for complete filling of the Sb dangling bonds. For higher Ti occupancies, the excess electrons are expected to destabilize the dimers and favor dehybridization into two dangling bonds per Sb atom: For this undimerized case with filled dangling bonds, the electron count predicts stability for $n_{Ti} = 7/8$.

Benchmarking the model

We use DFT calculations to test the predictions of the electron counting model: namely, that (i) surface dimers are stabilizing and (ii) a non-stoichiometric coverage of Ti is expected. First, we test the stabilizing effects of Sb-Sb dimerization. Figure 5B compares the DOS for two slabs with $n_{Ti} = 0$: one slab with atoms in their unrelaxed (undimerized) positions and the other where the structure is relaxed by dimerization. The DOS of the unrelaxed structure exhibits a sharp peak at the Fermi level, which we attribute primarily to Sb dangling bond states, and indicates an electronic instability. The stabilizing effect of dimerization is to reduce the DOS at the Fermi level (E_F) by hybridizing half of the dangling bonds into lower-lying Sb-Sb dimer states, resulting in a lower DOS at E_F for the dimerized surface. Dimerization is also characterized electronically by a splitting of the surface Sb 5s state near −9 eV, which by contrast, is singly peaked for undimerized surfaces. We explain this trend in terms of dehybridizing the dangling bonds into out-of-plane dangling orbitals (π) and in-plane bridge orbitals (σ) (note S2).

We now test the effects of Ti occupancy, for which our electron counting model predicts dimer stability at $n_{Ti} = 3/8$ (for half-filled dangling bonds). Figure 5C shows a histogram of the surface Sb-Sb nearest-neighbor distances versus n_{Ti} for the relaxed slabs, and Fig. 5D shows the corresponding projected DOSs. We find that our simple electron counting is in excellent quantitative agreement with the DFT calculations: For $n_{Ti} > 3/8$, the Sb-Sb length is near that of the bulk value (4.16 Å), and the low-lying Sb 5s states are singly peaked, indicating undimerized surfaces. But for $n_{Ti} \leq 3/8$, the electron counting condition for half-filled dangling bonds, there is a sharp cutoff below which the bond length drops to 3.3 Å and the Sb 5s states become doubly peaked, indicating the formation of stable Sb-Sb dimers.

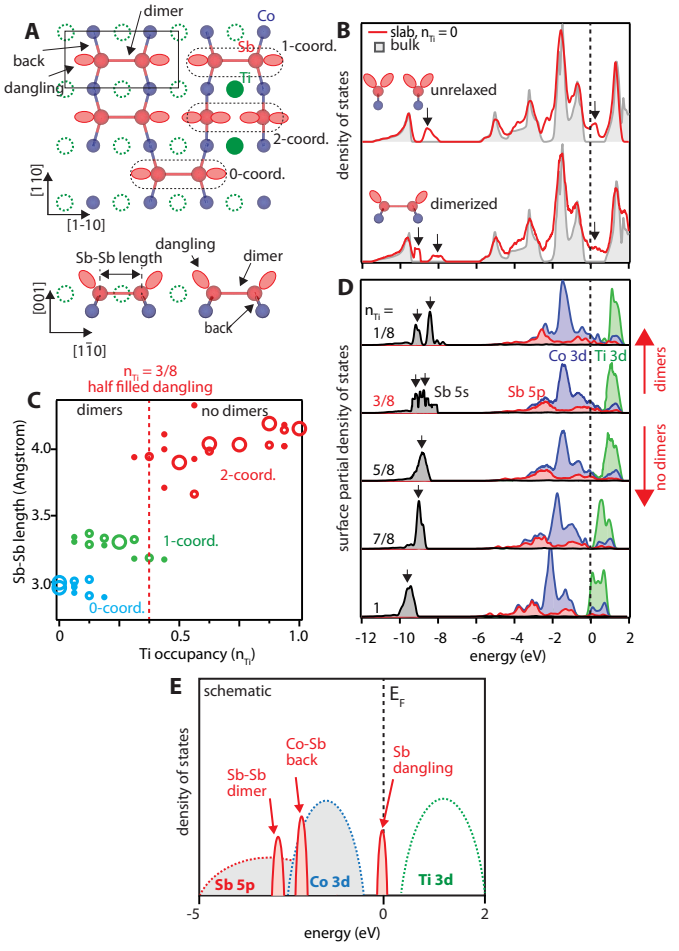

Fig. 5. Electron counting model. (**A**) Top-down and side views of a dimerized surface showing Ti vacancies (dashed circles), occupied Ti sites (filled green circles), and three types of bonds: Sb dangling, Sb-Sb dimer, and CoSb back. A (2 × 1) cell is outlined. (**B**) DOSs for unrelaxed versus dimerized slabs (red curves). The bulk DOS is shown for comparison (shaded gray). (**C**) Histogram of Sb-Sb bond length along the Sb dimer bond direction versus Ti occupancy (bin increment, 0.01 Å). The size of the symbol corresponds to occurrence of that bond length. (**D**) Projected DOS in the top two layers versus surface Ti occupancy, showing a splitting of Sb 5s states and rigid band shifts with Ti occupancy. (**E**) Schematic surface DOS. The Fermi level is sketched at half-filling of the Sb dangling bond states (n_{Ti} = 3/8).

Beyond the simple electron count, our DFT calculations also reveal that the Sb-Sb dimerization depends strongly on local Ti vacancy coordination. Each Sb-Sb pair can be coordinated with 0, 1, or 2 filled nearest-neighbor Ti sites along the [110] direction (Fig. 5A). The calculated Sb-Sb bond lengths cluster around discrete values based on this coordination: Sb-Sb pairs with twofold coordination have a pair length around 4.0 Å and are undimerized (Fig. 5C, red circles), pairs with onefold coordination have a bond length of 3.3 Å and are dimerized (green), and pairs with zero coordination have a bond length of 3.0 Å and are dimerized (blue). These trends can be seen directly in the relaxed atomic structures (fig. S5).

This strong dependence on local coordination may explain why n_{Ti} = 3/8 (half-filled dangling bonds) is the criteria for dimerization rather than n_{Ti} = 5/8 (filled dangling bond). For a given n_{Ti}, calculations over the various Ti coverage configurations reveal (i) that configurations with large separation between occupied Ti sites are energetically most favorable (to minimize the Coulomb repulsion ~ $\Sigma(1/r)$; fig. S5) and (ii) that Sb-Sb pairing favors sites coordinated with one Ti (to satisfy the local electron count). This presents a challenge for dimer formation on surfaces with $n_{Ti} > 1/2$. For example, for $n_{Ti} = 1/2$, the low-energy structure that minimizes the Coulomb repulsion consists of alternating [110]-oriented rows of occupied Ti sites and vacant Ti sites (fig. S5). Here, the Sb-Sb pairing prefers sites with nonzero Ti coordination, yet these sites with coordination 2 are too electron-rich to support a dimer and, instead, dehybridize into dangling bonds to accommodate the excess electrons. Hence, dimers in this configuration are not stable. Decreasing to $n_{Ti} \leq 3/8$ allows the conditions for (i) Coulomb repulsion and (ii) local coordination to be satisfied simultaneously. A summary of benchmarks between the electron counting model, experiment, and DFT is found in table S1.

The Ti occupancy also has a strong effect on the position of the Fermi level and pseudogap formation (Fig. 5D). With increasing n_{Ti} (electron doping), the Fermi level increases as expected, from the valence band edge for $n_{Ti} = 1/8$ to the conduction band edge for $n_{Ti} = 1$. For $n_{Ti} = 3/8$ (electron counting condition for dimerization), the Fermi level cuts through a band of Sb 5p dangling bond states, consistent with the finite spectral weight observed at E_F in our angle-integrated valence band measurements (Fig. 3B) and scanning tunneling spectroscopy measurements (Fig. 4). Hence, this surface is metallic. These metallic surface states persist for $n_{Ti} = 5/8$. At $n_{Ti} = 7/8$ a pseudogap appears at E_F, where the DOS goes to a sharp but finite minimum.

Electronic surface states

ARPES measurements on a $c(2 \times 4)$ sample confirm that the states within the bulk bandgap are two-dimensional metallic surface states, rather than defect states. Figure 6 (A and B) shows the measured in-plane dispersions at a fixed photon energy of 100 eV. This photon energy corresponds approximately to a slice at constant out-of-plane momentum $k_z = 4.96(2\pi/a)$, as determined from photon energy–dependent scans and using a free electron–like model of final states (see Materials and Methods and fig. S6). Peak fitting of the energy distribution curve (EDC) and momentum distribution curve (MDC) is shown in Fig. 6B (bottom). The measured dispersions below 0.6 eV are in general agreement with DFT-GGA calculations for bulk CoTiSb, both in terms of their qualitative dispersion and measured bandwidth (within 10%). Within the bulk gap (above 0.6 eV), we observe metallic states that are highly dispersive with in-plane momentum. Measurements at varying photon energy confirm that they are two-dimensional as they do not disperse with out-of-plane momentum (Fig. 6E and figs. S6 and S7). Hence, these in-gap states are surface states, rather than defect states that would be disordered (dispersionless). We attribute the metallic surface states to Sb dangling bonds, as identified by our slab calculations (Fig. 6C) and predicted by our electron counting model at half–Sb dangling bond filling (n_{Ti} = 3/8; Fig. 5E). The measured Fermi surface shown in Fig. 6D is characterized by hole pockets at (1, 0), (1, 1), and (0, 1/2) and, hence, follows the $c(2 \times 4)$ periodicity of the surface reconstruction, again confirming that the surface states are reconstruction-derived.

Implications for other Heuslers

The general framework used to unravel the atomic and electronic structure at the CoTiSb (001) surface provides an explanation for the structure and properties observed in other half-Heusler systems with the general formula *XYZ*. Half-Heuslers can generally be expressed as

an XZ^{n-} zincblende sublattice, stuffed with electropositive Y^{n+}. The Y^{n+} acts as a highly localized donor, whose concentration at the surface changes to maintain charge neutrality. The most electronegative Z atoms tend to dimerize to minimize the number of dangling bonds, and the filling of these dangling bonds is subject to the local electron count.

We first apply the framework to explain the surface behavior of NiMnSb (001), the canonical half-metallic ferromagnet. In the bulk, experiments confirm that NiMnSb is half-metallic with near 100% measured spin polarization (*26*). However, at the surface and at interfaces with III-V semiconductors, the spin polarization is often more than a factor of two smaller due to the presence of non–spin-polarized surface and interface states (*27*), which severely limits the performance of spin injection and magnetic tunnel junction–based devices. Experimentally, the (001) surface forms a (2 × 1) reconstruction, as measured by reflection high-energy electron diffraction (RHEED) during MBE growth (*11*), but depending on the postgrowth annealing conditions, the surface Mn concentration, reconstruction, and spin polarization can vary markedly (*12*).

We explain the origins of Mn nonstoichiometry and non–spin-polarized surface/interface states using our electron counting model. Here, $NiSb^{3-}$ forms the zincblende sublattice and the magnetic ion Mn^{3+} "stuff" at the octahedral sites. Therefore, the most electronegative Sb is expected to dimerize, and charge neutrality drives the formation of surface Mn vacancies. Application of the count suggests a stable Sb-Sb–dimerized surface for Mn coverage of n_{Mn} = 1/7 (half-filled dangling bonds) or n_{Mn} = 2/7 (filled dangling bonds). The combination of Mn vacancies and the existence of near E_F Sb dangling bond states then lead to decreased surface spin polarization, as the magnetic moment is carried on Mn^{3+} sites (*28*). Recent experiments have shown that, by intentionally depositing an excess ML of Mn on the (001) surface of the related full-Heusler Co_2MnSi, the spin polarization increases to nearly 90 % (*29*).

For the topological half-Heuslers Pt*LnV* (*Ln* = lanthanide metal, *V* = Sb or Bi), recent ARPES measurements confirm the existence of topological surface states (*4*), whose novel spin momentum locking is promising for applications in spintronics and quantum computing. Yet, the (001) surface also exhibits trivial surface states near the Fermi energy (*4*), which may act as parasitic conduction channels or even hybridize with topological states (*30*). Applying the model to the topological semimetal Pt*LnV* (001), PtV^{3-} makes the zincblende sublattice and Ln^{3+} stuffs. We expect group V dimer stability for n_{Ln} = 1/3 (half-filled dangling bonds) or n_{Ln} = 2/3 (filled dangling bonds). This is consistent with the $c(2 \times 2)$ surface of PtLuSb, for which recent x-ray photoelectron spectroscopy (XPS) measurements found evidence for Sb-Sb dimers (*31*). The previously observed trivial surface states (*4*) are likely of group V dangling bond origin but could be pushed significantly below E_F via control of the surface *Ln* concentration or surface electron doping, for example, via alkali metal deposition.

For the thermoelectric semiconductor NiTiSn, RHEED and LEED studies show that (001) surfaces exhibit a number of 2× reconstructions as a function of anneal temperature and Ti stoichiometry (*13*, *32*), consistent with Sn-Sn dimerization. Here, $NiSn^{4-}$ forms the zincblende sublattice, and Ti^{4+} stuff. Applying the electron count, we find stable surfaces with Sn-Sn dimerization for n_{Ti} = 1/2 (half-filled dangling bonds) and n_{Ti} = 3/4 (filled dangling bonds). An interesting feature

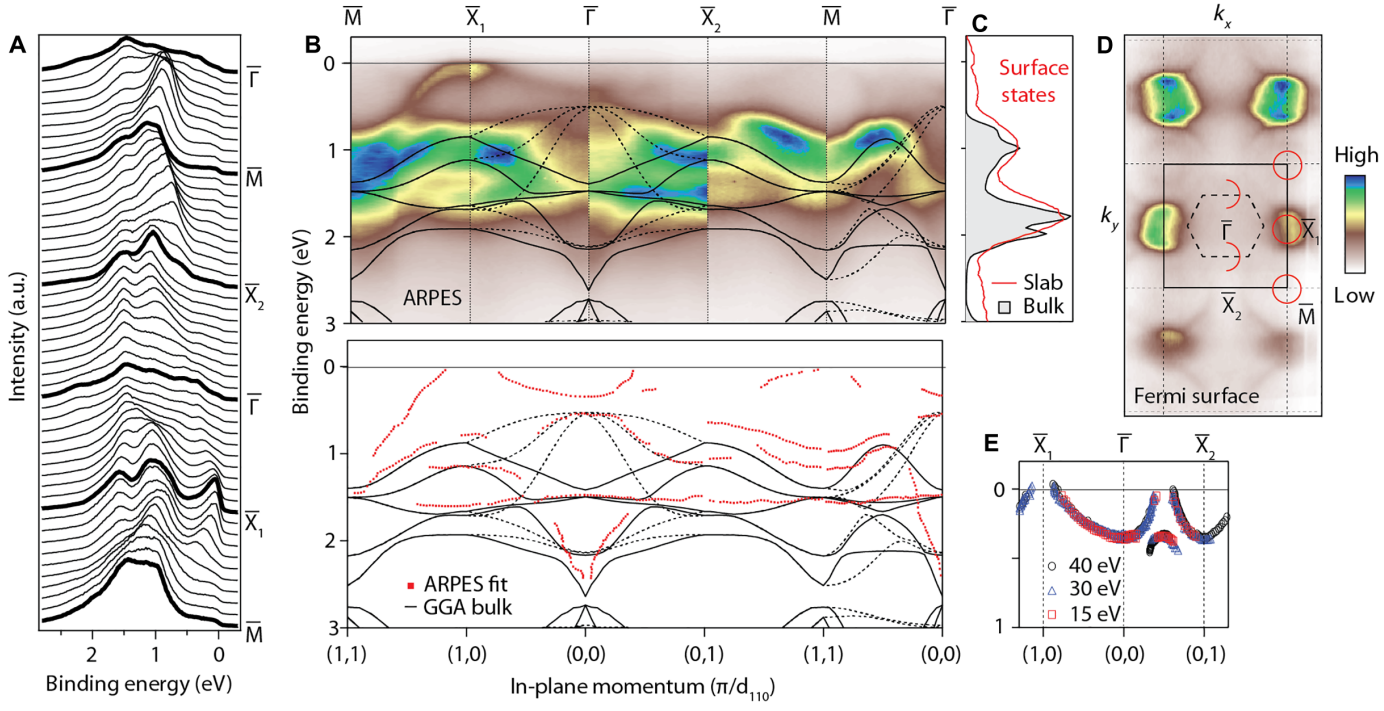

Fig. 6. In-plane dispersions and metallic surface states for *c*(2 × 4)-terminated CoTiSb (001). k_x||[–110] and k_y||[110]. (**A**) Energy dispersion curves at fixed photon energy of 100 eV. (**B**) Top: ARPES intensity map following the same dispersion as in (A). Bottom: MDC and EDC fitting of the ARPES dispersions (red dots) and comparison with DFT at constant $k_z = 4.96(2\pi/a)$ (black curves). Dashed black lines show the zone-folded DFT bands expected from surface Umklapp scattering. (**C**) Bulk and slab (n_{Ti} = 3/8) DFT DOSs. (**D**) Fermi surface measured at $h\nu$ = 100 eV showing a $c(2 \times 4)$ periodicity, overlaid with a schematic Fermi surface. (**E**) EDC and MDC fitting of the surface states at several photon energies demonstrating their two-dimensional dispersion.

of this system is the coexistence of the full-Heusler phase Ni_2TiSn with half-Heusler NiTiSn and a fairly large solubility of Ni in $Ni_{1+\delta}TiSn$ for δ up to 0.05 (*32*). We explain these features in an electron counting picture: In the compound, Ni has formal valence occupancy $3d^{10}$ and, hence, is charge-neutral (Ni^0). Therefore, adding excess Ni to the lattice does not change the total charge of the compound, and NiTiSn is expected to be more tolerant to changes in Ni stoichiometry than other Heusler systems for which the *X* site is not charge-neutral.

Finally, we caution that, while our electron counting model is simple and predictive, it is not deterministic. The choice of structure that satisfies electron counting is not unique, and there can be multiple structures that satisfy the criteria. Therefore, the model is best used as a simple procedure to efficiently screen among possible surface structures that are constrained by experimental data. It is then possible to check and refine select candidate structures with perturbative DFT methods. The guidance and physical intuition provided by our model are especially important since half-Heuslers are ternary compounds, with many more configurational degrees of freedom than simple binary semiconductors.

DISCUSSION

On the basis of a combination of experiment and first-principles calculations, we showed that the half-Heusler CoTiSb (001) surface exhibits a wide range of reconstructions as a result of two driving forces: (i) minimizing the number of energetically unfavorable dangling bonds and (ii) maintaining charge neutrality at the surface. The former occurs via *Z* site (Sb) dimerization or a *Z* adlayer, while the latter charge neutrality is maintained by reducing the electropositive *Y* site (Ti) stoichiometry at the surface. We developed a simple electron counting model that makes quantitatively accurate predictions for the CoTiSb surface, as benchmarked against experiments and DFT. This is somewhat surprising since CoTiSb is a p-d hybridized system, in contrast with the simple s-p bonding of conventional III-V and II-VI compound semiconductors. Our simple model also explains the previously observed behavior at other half-Heusler surfaces and provides a simple framework for understanding and predicting the atomic structure and properties of these novel quantum materials.

MATERIALS AND METHODS

MBE growth and surface termination

CoTiSb films with thickness of 20 to 40 nm were grown by molecular beam epitaxy (MBE) on $In_{0.52}Al_{0.48}As$ (400 nm)/InP:S (001). The InAlAs buffer layer was doped with approximately 10^{19} Si atoms/cm^3 to yield a conductive buffer for STM and photoemission measurements. The CoTiSb layer was grown at 400°C by codeposition from Co, Ti, and Sb effusion cell sources in a 1:1:1.2 flux ratio, as calibrated by beam flux ionization gauge and Rutherford backscattering spectrometry measurements. Here, we used the high relative volatility of Sb to enable growth with excess Sb in an adsorption-controlled regime. Further growth details are provided elsewhere (*14*). On some samples, a 3-nm ErAs diffusion barrier was grown between the CoTiSb and InAlAs layer to prevent interfacial reactions between the CoTiSb and InAlAs at elevated annealing temperatures.

After growth, the Co and Ti effusion cells were shuttered, and the samples were annealed as a function of temperature and Sb flux. We chose to anneal with an Sb flux because of the high relative volatility of Sb above 300°C. By contrast, the sticking coefficients for Ti and Co were near unity for growth and anneal temperatures below 1000°C. The periodicity of the reconstruction during the anneal procedure was monitored by reflection high energy electron diffraction (RHEED) (fig. S1). Following the anneal, the Sb cell was shuttered, and the sample was rapidly quenched to room temperature while monitoring the RHEED pattern to retain the desired surface reconstruction.

In situ LEED, STM, and XPS

In situ LEED, XPS (Al *Kα* source, $h\nu$ = 1486.3 eV), and scanning tunneling microscopy and spectroscopy (STM/STS) (Omicron VT-STM) were performed in an interconnected MBE surface analysis system such that growth and characterization were performed without removing samples from ultrahigh vacuum ($< 2 \times 10^{-10}$ torr). These measurements were performed at room temperature. STM measurements were performed using electrochemically polished W tips. Upon loading into vacuum, the W oxides were cracked by electron bombardment. Tunneling point spectroscopy was performed using a stabilization bias of −2 V and a stabilization current of 1.5 to 2 nA. The $dI/dV(V)$ curves were obtained by numerical differentiation of averages of at least 10 raw $I(V)$ curve (fig. S4).

Synchrotron photoemission

High-resolution core-level photoemission spectroscopy and ARPES measurements were performed at the MAX-LAB Synchrotron facility in Lund, Sweden (beamlines I311 and I4, respectively). Core levels were measured at room temperature using a Scienta SES 200 analyzer, and ARPES band dispersions were measured at 80 K using a SPECS Phoibos analyzer. To protect the sample surfaces, immediately following growth, an approximately 100-nm-thick Sb cap was deposited on the CoTiSb films at 200°C in the MBE chamber. Capped samples were then unloaded from the MBE and transported through air to the beamline. Upon reloading them into the vacuum at the beamline, the Sb cap was thermally desorbed at 450°C until the appearance of a $c(2 \times 4)$ reconstruction in LEED. The stoichiometry and surface cleanliness (lack of carbon and oxygen) were confirmed by core-level measurements and the sharpness of the LEED pattern. All binding energies were referenced to the Fermi level, as determined by measuring the Fermi level of a tantalum or gold foil that was in electrical contract with the sample.

XPS intensity calculation

The photoemission intensity I_x of an elemental core level *x* was modeled as the sum of exponentially attenuated intensities emanating from each atomic layer *i* (*33*). In the limit of a constant interlayer spacing d_i and uniform attenuation length λ_x through the material, the intensity is

$$I_x = f_x \sigma_x \sum_{i=0}^{N} n_{x,i} \exp\left(\frac{-Z_i}{\lambda_x \cos\phi}\right) \quad (1)$$

where f_x is an instrument-dependent factor, σ_x is the photoemission cross section, $n_{x,i}$ is the two-dimensional atomic density of element *x* in layer *i*, $Z_i = i \times d_i$ is the depth from the surface, ϕ is the emission angle off the surface normal, $i = 0$ indexes the surface, and $N \rightarrow \infty$ is the total number of atomic layers. Our measurements were performed at fixed $\phi = 55°$. The attenuation lengths for the Co 2p, Ti 2p, and Sb 3d were calculated to be 11.1, 15.1, and 14.2 Å, respectively, using the empirical TPP-2M model (*34*). In (001) orientation, bulk CoTiSb consists of alternating layers of TiSb and Co, that is, $n_{\mathrm{odd,Co}} = n_{\mathrm{even,Ti}} = n_{\mathrm{even,Sb}} = n_{\mathrm{ML}}$, $n_{\mathrm{even,Co}} = n_{\mathrm{odd,Ti}} = n_{\mathrm{odd,Sb}} = 0$, and $d_i = a_0/4$, where $a_0 = 5.88$ Å is the lattice constant and $n_{\mathrm{ML}} = 2/a_0^2$ is the elemental atomic ML density. In

our fits, we considered the case of Ti vacancy formation in the top-most TiSb layer, that is, $n_{0,\mathrm{Ti}} < n_{\mathrm{ML}}$, as well as an Sb adlayer on top of the TiSb.

For comparison with experiment, we canceled out the instrument-dependent factors, f_x, by considering the ratio of ratios, that is

$$\frac{(I_x/I_{\mathrm{Co}})_{n\times m}}{(I_x/I_{\mathrm{Co}})_{2\times 1}} = \frac{(f_x/f_{\mathrm{Co}})\sum(\cdots)_{n\times m}}{(f_x/f_{\mathrm{Co}})\sum(\cdots)_{2\times 1}} \quad (2)$$

where we first normalized to the intensity of Co, since Co is expected to be subsurfaced and less subjected to stoichiometry changes than the top-most, nominally TiSb-terminated layer. This is consistent with the MnSb (TiSn) termination for (001) surfaces of NiMnSb (NiTiSn) (*11*, *13*). We then normalized the I_x/I_{Co} ratio for the $(n \times m)$ reconstruction to that of the (2×1) to eliminate the instrument factor f_x/f_{Co}. Hence, the ratio of ratios represents the relative change in composition of species x in the $(n \times m)$ reconstruction compared to that of the (2×1).

ARPES free electron–like model

The out-of-plane momentum was determined using a free electron–like model of final states, $k_z = \sqrt{2m/\hbar^2}(E_{\mathrm{kin}}\cos^2\theta + U_0)^{1/2}$. This model contains a single adjustable parameter of the inner potential U_0, which we determined to be $U_0 = 12$ eV by matching the periodicity of the bands (fig. S6). This value is in agreement with typical values observed for fcc transition metals and III-V semiconductors [$U_0 = 10$ to 15 eV (*35*)].

Density functional theory

DFT calculations were based on the generalized Kohn-Sham theory (*36*) with GGA of Perdew, Burke, and Ernzerhof (*37*), as implemented in Vienna ab initio simulation package (*38*) and in Wien2k (*39*). The electronic structure of bulk CoTiSb is in agreement with previous studies (*40*). Tests using a hybrid functional to correct the bandgap indicated that the shape of the bands remained unchanged, except that the bandgap increased by 0.36 eV compared to the DFT-GGA calculations (fig. S3). The surface calculations were carried out using a slab model using $2 \times 2 \times 1$ mesh of special k-points in the Brillouin zone and 268-eV energy cutoff for plane wave expansion. The interactions between the valence electrons and the ionic cores were treated using the projector-augmented wave potentials. A 4×4 supercell with atomic 13 layers was used with two equivalent surface (top and bottom) rotated 90° from each other due to the symmetry of the zincblende sublattice. In all the calculations, the positions of the atoms in the innermost five layers of the slab were fixed to that of the bulk CoTiSb. The atoms near the surface in four layers of top and bottom surface were allowed to relax. We focused on nominally TiSb-terminated surfaces so that the ideal surface contains 16 Sb and 16 Ti atoms in the supercell, and we varied the composition and configuration of Ti vacancies in the top-most TiSb layer from $n_{\mathrm{Ti}} = 0$ (all vacancies) to $n_{\mathrm{Ti}} = 1$ (full occupancy). For $n_{\mathrm{Ti}} < 1$, the energy was minimized when the distances between occupied Ti-Ti sites were maximized.

SUPPLEMENTARY MATERIALS

Supplementary material for this article is available at http://advances.sciencemag.org/cgi/content/full/4/6/eaar5832/DC1

note S1. Orbital hybridization.
note S2. Dimer splitting of the Sb 5s states.
note S3. Band bending and Fermi-level pinning by surface states.
table. S1. Summary of benchmarks for the electron counting model, focusing on the Sb dimer (2×1) and $c(2 \times 4)$ reconstructions of CoTiSb (001).
fig. S1. RHEED, LEED, and raw XPS spectra.
fig. S2. Bulk bonding and band character for CoTiSb.
fig. S3. Comparison between experiment (valence band photoemission) and two levels of DFT: the GGA and a hybrid functional Heyd-Scuseria-Ernzerhof.
fig. S4. STM, line cuts, and raw I-V spectra.
fig. S5. DFT phase diagram and relaxed Ti configurations.
fig. S6. Out-of-plane k_z dispersions for $c(2 \times 4)$-terminated CoTiSb (001) for photon energies from 14 to 180 eV.
fig. S7. Low-energy ARPES measurements of surface states, with increased surface sensitivity.
fig. S8. Application of electron counting to screen possible (2×1) structures.

REFERENCES AND NOTES

1. A. Ohtomo, H. Y. Hwang, A high-mobility electron gas at the $LaAlO_3/SrTiO_3$ heterointerface. *Nature* **427**, 423–426 (2004).
2. S. Chadov, X. Qi, J. Kübler, G. H. Fecher, C. Felser, S. C. Zhang, Tunable multifunctional topological insulators in ternary Heusler compounds. *Nat. Mater.* **9**, 541–545 (2010).
3. H. Lin, L. A. Wray, Y. Xia, S. Xu, S. Jia, R. J. Cava, A. Bansil, M. Z. Hasan, Half-Heusler ternary compounds as new multifunctional experimental platforms for topological quantum phenomena. *Nat. Mater.* **9**, 546–549 (2010).
4. J. A. Logan, S. J. Patel, S. D. Harrington, C. M. Polley, B. D. Schultz, T. Balasubramanian, A. Janotti, A. Mikkelsen, C. J. Palmstrøm, Observation of a topologically non-trivial surface state in half-Heusler PtLuSb (001) thin films. *Nat. Commun.* **7**, 11993 (2016).
5. R. A. de Groot, F. M. Mueller, P. G. van Engen, K. H. J. Buschow, New class of materials: Half-metallic ferromagnets. *Phys. Rev. Lett.* **50**, 2024 (1983).
6. K. Ullakko, J. K. Huang, C. Kantner, R. C. O'Handley, V. V. Kokorin, Large magnetic-field-induced strains in Ni_2MnGa single crystals. *Appl. Phys. Lett.* **69**, 1966 (1996).
7. Z. H. Liu, M. Zhang, Y. T. Cui, Y. Q. Zhou, W. H. Wang, G. H. Wu, X. X. Zhang, G. Xiao, Martensitic transformation and shape memory effect in ferromagnetic Heusler alloy Ni_2FeGa. *Appl. Phys. Lett.* **82**, 424 (2003).
8. Y. Nakajima, R. Hu, K. Kirshenbaum, A. Hughes, P. Syers, X. Wang, K. Wang, R. Wang, S. R. Saha, D. Pratt, J. W. Lynn, J. Paglione, Topological *R*PdBi half-Heusler semimetals: A new family of noncentrosymmetric magnetic superconductors. *Sci. Adv.* **1**, e1500242 (2015).
9. Z. Wang, M. G. Vergniory, S. Kushwaha, M. Hirschberger, E. V. Chulkov, A. Ernst, N. P. Ong, R. J. Cava, B. A. Bernevig, Time-reversal-breaking Weyl fermions in magnetic Heusler alloys. *Phys. Rev. Lett.* **117**, 236401 (2016).
10. C. Palmstrøm, Epitaxial Heusler alloys: New materials for semiconductor spintronics. *MRS Bull.* **28**, 725–728 (2003).
11. P. Bach, A. S. Bader, C. Rüster, C. Gould, C. R. Becker, G. Schmidt, L. W. Molenkamp, W. Weigand, C. Kumpf, E. Umbach, R. Urban, G. Woltersdorf, B. Heinrich, Molecular-beam epitaxy of the half-Heusler alloy NiMnSb on (In,Ga)As/InP (001). *Appl. Phys. Lett.* **83**, 521 (2003).
12. D. Ristoiu, J. P. Nozières, C. N. Borca, T. Komesu, H.-k. Jeong, P. A. Dowben, The surface composition and spin polarization of NiMnSb epitaxial thin films. *Europhys. Lett.* **49**, 624 (2000).
13. J. K. Kawasaki, T. Neulinger, R. Timm, M. Hjort, A. A. Zakharov, A. Mikkelsen, B. D. Schultz, C. J. Palmstrøm, Epitaxial growth and surface studies of the Half Heusler compound NiTiSn (001). *J. Vac. Sci. Technol. B* **31**, 04D106 (2013).
14. J. K. Kawasaki, L. I. M. Johansson, B. D. Schultz, C. J. Palmstrøm, Growth and transport properties of epitaxial lattice matched half Heusler CoTiSb/InAlAs/InP(001) heterostructures. *Appl. Phys. Lett.* **104**, 022109 (2014).
15. S. J. Patel, J. K. Kawasaki, J. Logan, B. D. Schultz, J. Adell, B. Thiagarajan, A. Mikkelsen, C. J. Palmstrøm, Surface and electronic structure of epitaxial PtLuSb (001) thin films. *Appl. Phys. Lett.* **104**, 201603 (2014).
16. Z. Zhu, H. Wang, U. Schwingenschlögl, Surface electronic states of 18 valence electron half-Heusler semiconductors. *Adv. Mater. Interfaces* **2**, 1400340 (2015).
17. J. M. K. Al-zyadi, M. H. Jolan, K.-L. Yao, Surface half-metallicity of half-Heusler compound FeCrSe and interface half-metallicity of FeCrSe/GaP. *J. Magn. Magn. Mater.* **403**, 8–13 (2016).
18. M. D. Pashley, Electron counting model and its application to island structures on molecular-beam epitaxy grown GaAs(001) and ZnSe(001). *Phys. Rev. B* **40**, 10481–10487 (1989).
19. F. Bechstedt, *Principles of Surface Physics* (Springer, 2003).
20. H. C. Kandpal, C. Felser, R. Seshadri, Covalent bonding and the nature of band gaps in some half-Heusler compounds. *J. Phys. D Appl. Phys.* **39**, 776 (2006).
21. D. Jung, H.-J. Koo, M.-H. Whangbo, Study of the 18-electron band gap and ferromagnetism in semi-Heusler compounds by non-spin-polarized electronic band structure calculations. *J. Mol. Struct. Theochem* **527**, 113–119 (2000).
22. S. Öğüt, K. M. Rabe, Band gap and stability in the ternary intermetallic compounds Ni*Sn**M* (*M*=Ti,Zr,Hf): A first-principles study. *Phys. Rev. B* **51**, 10443 (1995).
23. S.-C. Wu, S. S. Naghavi, G. H. Fecher, C. Felser, A critical study of the elastic properties and stability of Heusler compounds: Cubic Co_2YZ compounds with $L2_1$ structure. arXiv:1704.01752 (2017).

24. G. E. Franklin, D. H. Rich, A. Samsavar, E. S. Hirschorn, F. M. Leibsle, T. Miller, T.-C. Chiang, Photoemission and scanning-tunneling-microscopy study of GaSb(100). *Phys. Rev. B* **41**, 12619 (1990).
25. R. A. Wolkow, Direct observation of an increase in buckled dimers on Si(001) at low temperature. *Phys. Rev. Lett.* **68**, 2636–2639 (1992).
26. K. E. H. M. Hanssen, P. E. Mijnarends, L. P. L. M. Rabou, K. H. J. Buschow, Positron-annihilation study of the half-metallic ferromagnet NiMnSb: Experiment. *Phys. Rev. B* **42**, 1533–1540 (1990).
27. J. J. Attema, G. A. de Wijs, R. A. de Groot, The continuing drama of the half-metal/semiconductor interface. *J. Phys. D Appl. Phys.* **39**, 793 (2006).
28. I. Galanakis, P. H. Dederichs, N. Papanikolaou, Slater-Pauling behavior and origin of the half-metallicity of the full-Heusler alloys. *Phys. Rev. B* **66**, 174429 (2002).
29. S. Andrieu, A. Neggache, T. Hauet, T. Devolder, A. Hallal, M. Chshiev, A. M. Bataille, P. Le Fèvre, F. Bertran, Direct evidence for minority spin gap in the Co_2 MnSi Heusler compound. *Phys. Rev. B* **93**, 094417 (2016).
30. H. Lin, T. Das, Y. Okada, M. C. Boyer, W. D. Wise, M. Tomasik, B. Zhen, E. W. Hudson, W. Zhou, V. Madhavan, C.-Y. Ren, H. Ikuta, A. Bansil, Topological dangling bonds with large spin splitting and enhanced spin polarization on the surfaces of Bi_2Se_3. *Nano Lett.* **13**, 1915–1919 (2013).
31. S. J. Patel, J. A. Logan, S. D. Harrington, B. D. Schultz, C. J. Palmstrøm, Surface reconstructions and transport of epitaxial PtLuSb (001) thin films grown by MBE. *J. Cryst. Growth* **436**, 145–149 (2016).
32. A. D. Rice, J. K. Kawasaki, N. Verma, D. J. Pennachio, B. D. Schultz, C. J. Palmstrøm, Structural and electronic properties of molecular beam epitaxially grown $Ni_{1+x}TiSn$ films. *J. Cryst. Growth* **467**, 71–76 (2017).
33. A. K. Livesey, G. C. Smith, The determination of depth profiles from angle-dependent XPS using maximum entropy data analysis. *J. Electron Spectros. Relat. Phenomena* **67**, 439–461 (1994).
34. S. Tanuma, C. J. Powell, D. R. Penn, Calculation of electron inelastic mean free paths (IMFPs) VII. Reliability of the TPP-2M IMFP predictive equation. *Surf. Interface Anal.* **35**, 268–275 (2003).
35. P. Hofmann, C. Søndergaard, S. Agergaard, S. V. Hoffmann, J. E. Gayone, G. Zampieri, S. Lizzit, A. Baraldi, Unexpected surface sensitivity at high energies in angle-resolved photoemission. *Phys. Rev. B* **66**, 245422 (2002).
36. P. Hohenberg, W. Kohn, Inhomogeneous electron gas. *Phys. Rev.* **136**, B864 (1964).
37. J. P. Perdew, K. Burke, M. Ernzerhof, Generalized gradient approximation made simple. *Phys. Rev. Lett.* **77**, 3865–3868 (1996).
38. G. Kresse J. Furthmüller, Efficiency of ab-initio total energy calculations for metals and semiconductors using a plane-wave basis set. *Comput. Mater. Sci.* **6**, 15–50 (1996).
39. P. Blaha, K. Schwarz, G. K. H. Madsen, D. Kvasnicka, J.Luitz, "WIEN2K: An augmented plane wave plus local orbitals program for calculating crystal properties" (Technische Universität Wien, 2001).
40. J. Yang, H. Li, T. Wu, W. Zhang, L. Chen, J. Yang, Evaluation of half-Heusler compounds as thermoelectric materials based on the calculated electrical transport properties. *Adv. Funct. Mater.* **18**, 2880–2888 (2008).

Acknowledgments: We acknowledge S. Patel, A. Roy, and D. Fredrickson for the discussions and J. Adell for the beamline support at MAX-LAB. **Funding:** Sample fabrication at University of California, Santa Barbara and theory at the University of Delaware were supported by the U.S. Department of Energy under award number DE-SC0014388. Computer time was supported by the Extreme Science and Engineering Discovery Environment, NSF grant number ACI-1053575, and by the high-performance computing and the Information Technologies resources at the University of Delaware. Data analysis at the University of Wisconsin was supported by the Wisconsin Alumni Research Foundation and the NSF through the University of Wisconsin Materials Research Science and Engineering Center (Seed Project; NSF DMR-1121288). Travel for synchrotron beam time supported by NSF Nordic Research Opportunity. The work carried out at the MAX IV Laboratory was made possible through the support from the Swedish Research Council and the Knut and Alice Wallenberg Foundations. **Author contributions:** C.J.P. and J.K.K. conceived the project. J.K.K., L.I.M.J., and C.J.P. fabricated the samples. J.K.K., L.I.M.J., M.H., B.T., R.T., and A.M. performed the XPS and ARPES measurements. J.K.K., L.I.M.J., and B.D.S. performed the STM measurements. A.S., A.J., and J.K.K. performed the DFT calculations. J.K.K. wrote the manuscript, with help from A.J., A.S., and C.J.P. J.K.K. was responsible for checking all figures and text in both the main text and the Supplementary Materials. All authors contributed to the editing of the manuscript. **Competing interests:** The authors declare that they have no competing interests. **Data and materials availability:** All data needed to evaluate the conclusions in the paper are present in the paper and/or the Supplementary Materials. Additional data related to this paper may be requested from the authors.

Submitted 24 November 2017
Accepted 20 April 2018
Published 1 June 2018
10.1126/sciadv.aar5832

Citation: J. K. Kawasaki, A. Sharan, L. I. M. Johansson, M. Hjort, R. Timm, B. Thiagarajan, B. D. Schultz, A. Mikkelsen, A. Janotti, C. J. Palmstrøm, A simple electron counting model for half-Heusler surfaces. *Sci. Adv.* **4**, eaar5832 (2018).